

# CMS Draft Analysis Note

*The content of this note is intended for CMS internal use and distribution only*

2010/05/16

Head Id: 5564

Archive Id: 5736M

Archive Date: 2010/04/30

Archive Tag: trunk

## Transverse Momentum Distribution within Jets in pp Collisions at $\sqrt{s}=7$ TeV

Anwar A Bhatti<sup>1</sup>, Vivain, O'Dell<sup>2</sup>, Kenichi Hatakeyama<sup>3</sup>, Ozdemir Kadri<sup>4</sup>, and Pelin Kurt<sup>5</sup>

<sup>1</sup> The Rockefeller University, New York, NY 10065, USA

<sup>2</sup> Fermi National Accelerator Laboratory, Batavia IL 60510, USA

<sup>3</sup> Baylor University, Waco, TX 76706, USA

<sup>4</sup> Cukurova University, Adana, Turkey

<sup>5</sup> Vanderbilt University, Nashville, TN 37235, USA

### Abstract

Using  $pp$  collisions at center of mass energy of 7 TeV collected by CMS detector at Large Hadron Collider at CERN, we have measured the jet shapes, defined as the fractional transverse momentum distribution as a function of the distance from the jet axis. Since jet shapes are sensitive to parton showering processes they provide a good test of Monte Carlo event simulation programs. In this note we present a study of jet shapes reconstructed using calorimeter energies using CMS dataset with  $1 \text{ pb}^{-1}$  of integrated luminosity. We compare the results with predictions of the QCD inspired event generators PYTHIA and HERWIG++. For Pythia predictions, various underlying event tunes were studied and find that the **CW tune** best describes the data.

This box is only visible in draft mode. Please make sure the values below make sense.

PDFAuthor: Anwar Bhatti

PDFTitle: Transverse Momentum Distribution within Jets in pp Collisions at  $s=7$  TeV

PDFSubject: CMS

PDFKeywords: CMS, physics

Please also verify that the abstract does not use any user defined symbols



## Contents

1			
2	1	Introduction . . . . .	1
3	2	CMS Detector . . . . .	2
4	3	Jet Clustering Algorithms . . . . .	5
5	4	Data sets and luminosity . . . . .	5
6	4.1	Collider data . . . . .	5
7	4.2	Monte Carlo data . . . . .	6
8	5	Analysis . . . . .	6
9	5.1	Software . . . . .	6
10	5.2	Missing $E_T$ Significance . . . . .	6
11	5.3	Vertex Selection Criteria . . . . .	6
12	5.4	Jet Quality Requirements (Loose JetID) . . . . .	6
13	5.5	Track Selection . . . . .	6
14	5.6	Towers Selection . . . . .	7
15	6	Multiplicity of Jet Constituents . . . . .	7
16	7	$p_T$ Distributions of Particles, Tracks and Towers in a Jet . . . . .	7
17	8	Definition of Jet Shapes . . . . .	11
18	9	Raw Jet Shapes . . . . .	12
19	10	Jet Shape Corrections . . . . .	12
20	11	Corrected Jet Shapes . . . . .	15
21	12	Sensitivity of Jet Shapes to Underlying Event Tunes . . . . .	16
22	13	Quark and Gluon Jet Shapes . . . . .	16
23	14	Systematic Uncertainties . . . . .	17
24	14.1	Jet Energy Scale . . . . .	18
25	14.2	Jet Fragmentation . . . . .	18
26	14.3	Non-linearity of Calorimeter Response and Transverse Shower Profile . . . . .	19
27	15	Conclusions . . . . .	19

## 1 Introduction

The transverse momentum profile of a jet, jet shapes [1, 2], is sensitive to multiple parton emissions from the primary outgoing parton and provides a good test of the parton showering description of Quantum Chromodynamics (QCD), the theory of strong interactions. Historically the jet shape has been used to test perturbative QCD (pQCD)  $\alpha_s^3$  calculations [3, 4]. These leading order calculations, with only one additional parton in a jet, showed good agreement with the observed jet shapes. While confirming the validity of pQCD calculations, jet shape studies also indicated that jet clustering, underlying event contribution and hadronization effects must be considered. Currently, these effects can be modeled accurately only within the framework of full-event generators. Current Monte Carlo (MC) event generators use pQCD inspired parton shower models, in conjunction with hadronization and underlying event models, to generate final state particles. MC generators are used extensively to model signal and background events in most analyses at hadron colliders. Jet shapes can be used to tune phenomenological parameters in these MC generators. QCD predicts broader gluon jets than quark jets. The structure of quark and gluon jets can be investigated by comparing measurements of the jet shapes in different processes enriched with either quark or gluon initiated jets in the final state.

44 In QCD jet production, the gluon jet contribution changes with the transverse momenta of the  
 45 jets. Previously, jet shapes have been measured in  $p\bar{p}$  collisions at Tevatron and  $ep$  collisions at  
 46 HERA [3–7]. In this paper, we present a study of jet shapes measured using calorimeter infor-  
 47 mation in the central region of the CMS detector at  $\sqrt{s} = 7$  TeV using integrated luminosity of  
 48  $1.0 \text{ nb}^{-1}$ , and compare the results obtained with various MC generators. The sensitivities of  
 49 jet shapes to the underlying event (UE) model and to the flavor of the initiating parton are also  
 50 explored.

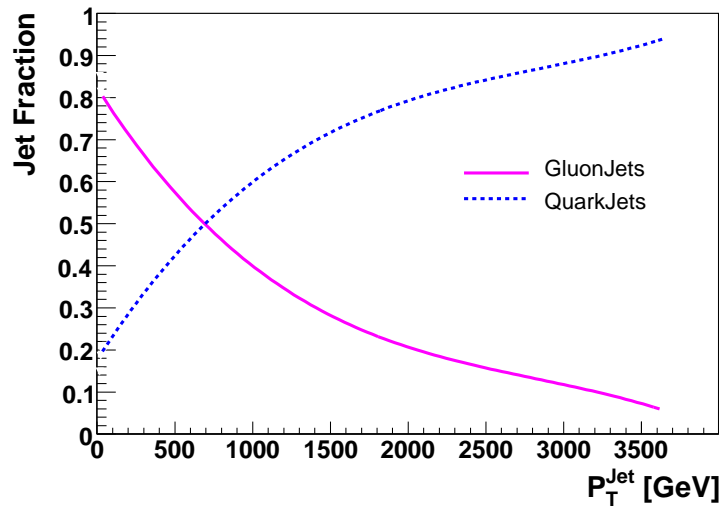


Figure 1: Fraction of the quark or gluon initiated jets as a function of jet  $p_T$  for  $|y| < 1$  (from PYTHIA DWT).

## 51 2 CMS Detector

52 The Compact Muon Solenoid (CMS) detector is a multipurpose apparatus at the Large Hadron  
 53 Collider (LHC) at CERN. The CMS has a cylindrical structure covering almost  $4\pi$  of angular  
 54 phase-space in order to detect a large fraction of particles produced in a  $pp$  collision. It con-  
 55 tains subsystems which are designed to measure energies and momenta of photons, electrons,  
 56 muons, and hadrons [8–10].

57 The central hadronic section (HCAL) is made of brass and scintillators while the electromag-  
 58 netic section (ECAL) comprises lead tungstate crystals ( $PbWO_4$ ). The response of the calorime-  
 59 ter to photons is linear versus incident energy, while the response to hadrons depends strongly  
 60 on the incident energy. The difference in response of the calorimeter to photons and hadrons  
 61 leads to a nonlinear energy response of the calorimeter to jets.

62 The coordinate system used at CMS[11] is defined as follows: the  $x$ -axis points horizontally  
 63 outside the LHC ring, the  $y$ -axis points upwards, and the  $z$ -axis is aligned with the nominal  
 64 clock-wise beam direction. The azimuthal angle is  $\phi$  and the polar angle is  $\theta$ . The transverse  
 65 momentum  $p_T$  is defined as a projection of a particle momentum  $P$  on the  $xy$ -plane,  $p_T =$   
 66  $P \cdot \sin \theta$ , and the “transverse energy” as  $E_T = E \cdot \sin \theta$ . The rapidity is defined as  $y = \frac{1}{2} \log \frac{E+P_Z}{E-P_Z}$ ,  
 67 where  $E$  denotes the energy and  $P_Z$  is the component of the momentum along the  $z$  direction.  
 68 The pseudo-rapidity is defined as  $\eta = -\ln[\tan \frac{\theta}{2}]$ .

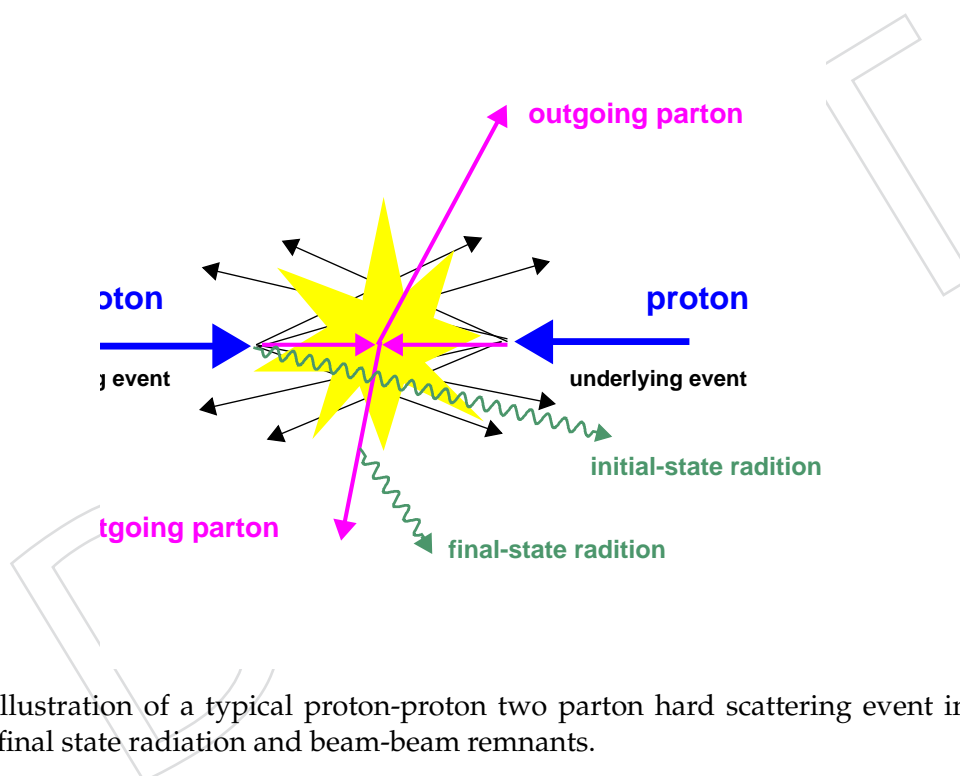


Figure 2: Illustration of a typical proton-proton two parton hard scattering event including initial and final state radiation and beam-beam remnants.

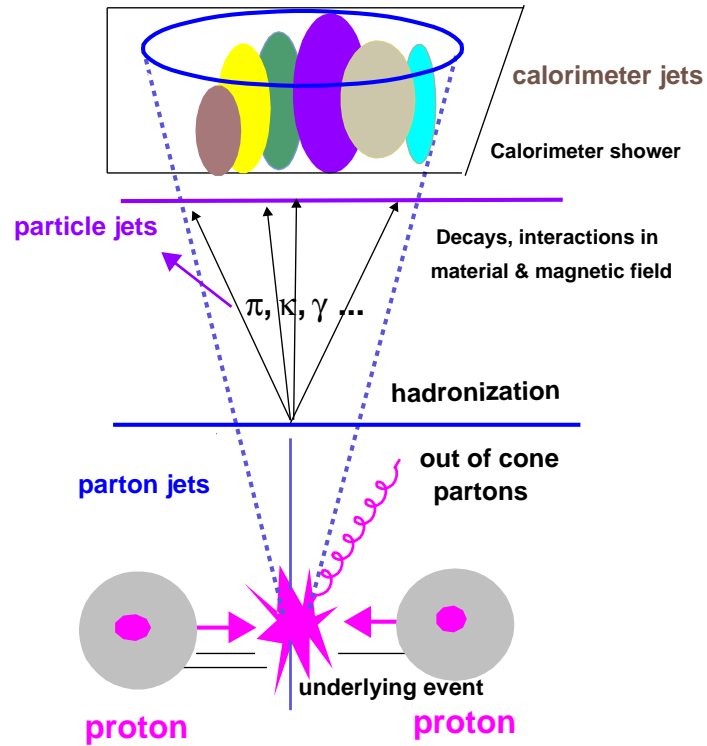


Figure 3: Schematic of jet evolution and detection. Parton jets hadronize into particle jets which interact in the calorimeter forming calorimeter jets.

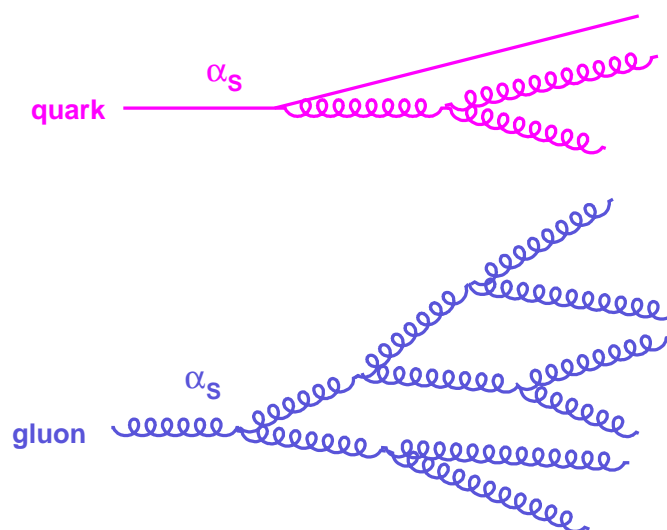


Figure 4: Examples of the structure of quark and gluon initiated jets

### 3 Jet Clustering Algorithms

In high energy interactions partons are produced in the final state with large transverse momenta as a result of the hard scattering process illustrated in Figure 2. Partons outgoing from the interaction point produce parton showers and subsequently partons from these showers combine to form hadrons which are color singlets which interact in the detector (see Figure 3). Since the transverse momenta involved in the hadronization process are much smaller than the hard scattering momenta, the final state particles are collimated around the direction of the original parton. These streams of particles are called jets. Jet clustering algorithms are used to associate particles to a particular jet. Direction and energy of a jet are related to the direction and energy of the original parton.

Many jet reconstruction algorithms are being used in CMS including iterative cone,  $k_T$ , SIS-Cone (Seedless Infrared Safe Cone) [12] and anti- $k_T$  algorithms [13]. The cone jet algorithm, such as SIS-Cone, groups the input objects together based on their distance in  $(y, \phi)$  space, and the determination of the jet quantities is done at the end of the jet finding. The successive recombination algorithms iteratively merge input objects into final jets and so the jet kinematic quantities, the jet direction and energy, are calculated directly during the clustering. In this analysis, the anti- $k_T$  algorithm has been used to reconstruct jets with  $D = 0.7$ . The anti- $k_T$  algorithm [13] starts with a list of proto-jets given by 4-momentum  $(E, p_x, p_y, p_z)$ . All the objects which are to be clustered are considered as proto-jets. The transverse momentum  $p_T$ , rapidity  $y$ , and azimuthal angle  $\phi$  of a proto-jet are calculated using give Equation 2.

$$(E, p_x, p_y, p_z) = \sum_i (E, p_x, p_y, p_z)_i \quad (1)$$

$$p_T = \sqrt{p_x^2 + p_y^2} \quad y_c = \frac{1}{2} \ln \left( \frac{E + p_z}{E - p_z} \right) \quad \phi_c = \tan^{-1}(p_y/p_x). \quad (2)$$

For each proto-jet  $i$  and the pair  $(i, j, i \neq j)$ ,  $d_i$  and  $d_{ij}$  are defined as

$$d_i = p_{T,i}^2 \quad d_{ij} = \min(p_{T,i}^{2p}, p_{T,j}^{2p}) \frac{(y_i - y_j)^2 + (\phi_i - \phi_j)^2}{D^2} \quad (3)$$

where  $D$  is the parameter which controls the size of the jet. For the anti- $k_T$  algorithm, the parameter  $p = -1$ . The algorithm determines the minimum  $d_{min}$  of the  $d_i$  and all the  $d_{ij}$ . If  $d_{min} = d_i$ , the proto-jet is not mergable and is promoted to a jet. Otherwise, the proto-jets  $i, j$  are merged into a single proto-jet with the 4-momentum  $(E_{ij}, \vec{p}_{ij}) = (E_i + E_j, \vec{p}_i + \vec{p}_j)$ . The process is repeated until no proto-jets are left. In anti- $k_T$  algorithm the measure  $d$  depends on the  $1/p_T^2$  of the object, clustering the high  $p_T$  objects first. This procedure leads to a circular jets.

## 4 Data sets and luminosity

### 4.1 Collider data

The data collected with minimum bias and jet triggers is used. Currently using Run 132601. and require that event pass bit 40 or bit 41. In addition, the event is required to be in-time with beam crossing by requiring the BPTX bit to be set. The lumi sections in range 261-1131 are used. The events which pass any of the Beam Halo triggers labeled by bits 36,37, 38, 39 are rejected. These halo rejection and timing requirements remove most of the non-physics background from the data. In addition, the "Monster events" were explicitly removed. These monster events are high track multiplicity events which are related with the beam but not with

Figure 5:  $\cancel{E}_T$ ,  $\cancel{E}_T/\sum E_T$  and  $\cancel{E}_T$  significance  $\cancel{E}_T/\sqrt{\sum E_T}$  distributions in the data

94 the  $pp$  collisions close to the center of detector. Events were required to have at least one good  
95 primary vertex vertex. The vertex selection cuts are given in Section 5.3.

96 The data sets used in this analysis are:

dataset	Name (RECO)	Number of events	Integrated Luminosity
Data	/MinimumBias/Commissioning10-April-PromptReco-v8/		

## 99 4.2 Monte Carlo data

100 For QCD predictions we used PYTHIA event generator. Various data sets used are given below.

dataset	Name (GEN-SIM-RECO)	Cross section	Effective Luminosity
Pythia	/MinimumBias/Spring10-START3X.V26A.356ReReco-v1/		
Herwig	/MinimumBias/Spring10-START3X.V26A.356ReReco-v1/		

# 103 5 Analysis

## 104 5.1 Software

105 We use CMSSW version xxx.

## 106 5.2 Missing $E_T$ Significance

107 Figure 5 shows the distribution for  $\cancel{E}_T/\sum E_T$  in data compared to minimum bias data.

## 108 5.3 Vertex Selection Criteria

109 We follow the CMS recommendations and use following cuts

Number of degrees of freedom	$\text{ndof} > 5$
$z$ position of the vertex	$ z  < 15 \text{ cm}$
Radial position of the vertex	$\sqrt{x^2 + y^2} < 2 \text{ cm}$

## 111 5.4 Jet Quality Requirements (Loose JetID)

Energy fraction observed in EM calorimeter	$\text{emf} > 0.01$ if the $ \eta^{\text{jet}}  < 2.6$
Number of hits containing $\geq 90\%$ of the jet energy	$\text{n90Hits} > 2$
Fraction of the jet energy contained in a single HPD	$\text{fHPD} < 0.98$

## 113 5.5 Track Selection

114 We use For tracking study we use high quality tracks. In addition we require that reach track  
115 has at least six valid hits ( $\text{nValidHits} \geq 6$ ). We use track with  $p_T \geq 0.3 \text{ GeV}$ .

High purity tracks	Yes
$p_T$	$\geq 0.3 \text{ GeV}$
$\text{nValidHits}$	$\geq 6$
$\sigma(p_T)/p_T$	$\leq 5$ (need to add)
$(z - z_{\text{vertex}})/\sigma(z - z_{\text{vertex}})$	$\leq 5$ (need to add)
$(d - d_{\text{vertex}})/\sigma\Delta_d$	$\leq 5$ (need to add)

Figure 6: Number of towers, tracks in a jets as a function of jet  $p_T$ .

## 117 5.6 Towers Selection

118 To calculate the jetshapes, we used calorimeter towers with  $p_T > 0.3$  GeV. The towers are  
119 constructed from electromagnetic calorimeter cells (crystals) and hadron calorimeter cells us-  
120 ing Scheme 6 thresholds. In this scheme hadron calorimeter cell with energy  $> 0.xx$  GeV are  
121 included. For EM calorimeter crystals, each crystal is required to have energy above 0.090  
122 GeV and sum of 25 crystals contributing to a tower must be above 0.2 GeV. The ECAL crystals  
123 are readout using a selective readout scheme i.e. all crystal in 5x5 region around a cell of inter-  
124 est are readout without any zero-suppression threshold. If there is no cell of interest, only the  
125 cell with  $p_T > 1000$  GeV are readout.

## 126 6 Multiplicity of Jet Constituents

127 Figure 6 summarizes the mean multiplicities of particles, tracks and calorimeter towers in a  
128 jet as a function of jet  $p_T$ . As expected, they increase logarithmically with increasing jet  $p_T$ .  
129 Figures 9, 7 and 8 present the multiplicity distributions for particles, calorimeter towers and  
130 tracks in a jet, respectively, in selected  $p_T$  bins. The data are compared with the MC predictions  
131 and shows a good agreement.

## 132 7 $p_T$ Distributions of Particles, Tracks and Towers in a Jet

133  $p_T$  distributions of particles, tracks and towers in a jet are shown in Figures 10, 12 and 11,  
134 respectively. These distributions become harder with increasing jet  $p_T$ .

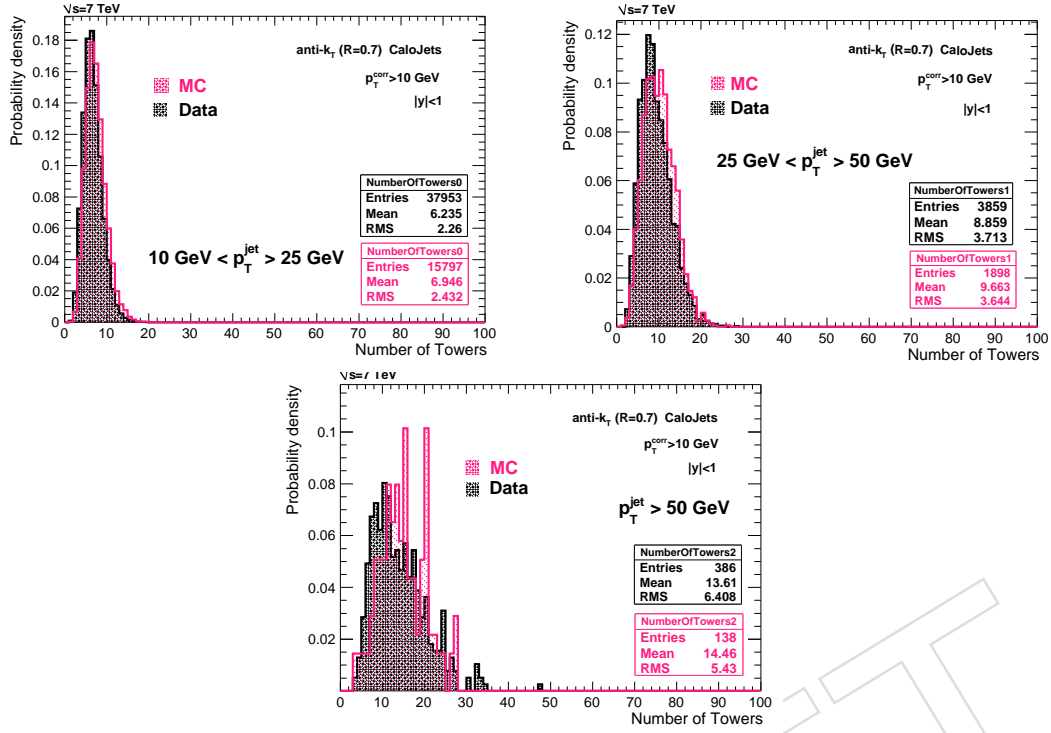


Figure 7: Number of towers with  $R = 0.7$  of the jet axis in bins of  $p_T$  of the jet in CMS data at  $\sqrt{s} = 7$

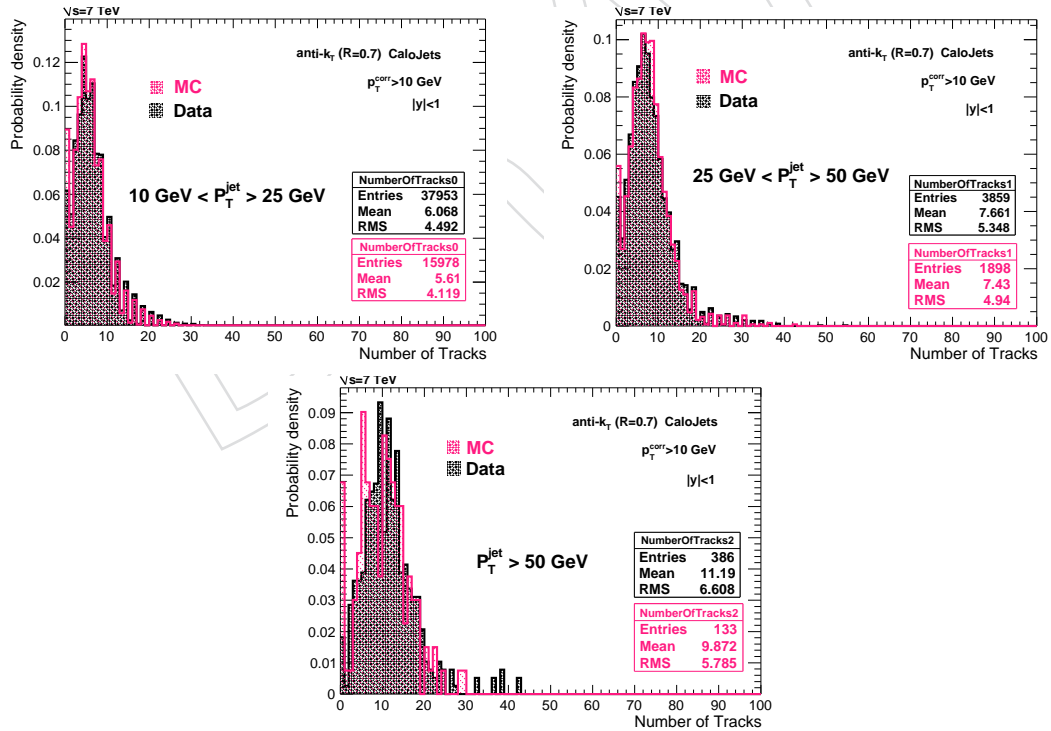


Figure 8: Number of good tracks with  $R = 0.7$  of the jet axis in bins of  $p_T$  of the jet in CMS data at  $\sqrt{s} = 7$

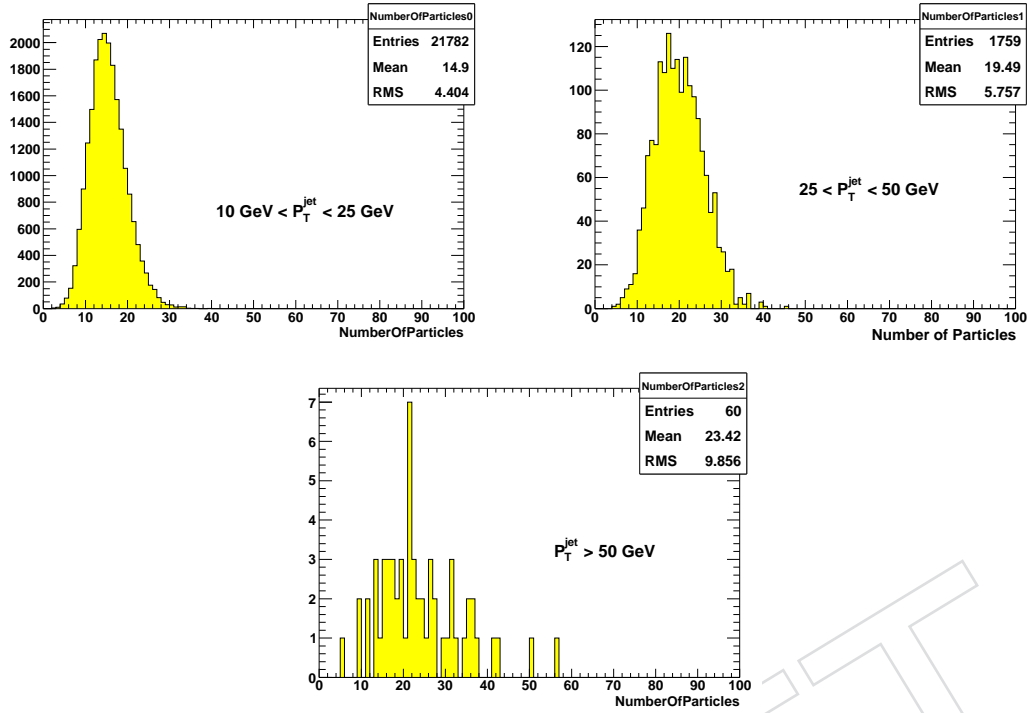


Figure 9: Number of particles with  $R = 0.7$  of the jet axis in bins of  $p_T$  of the jet in PYTHIA MC QCD multijet events

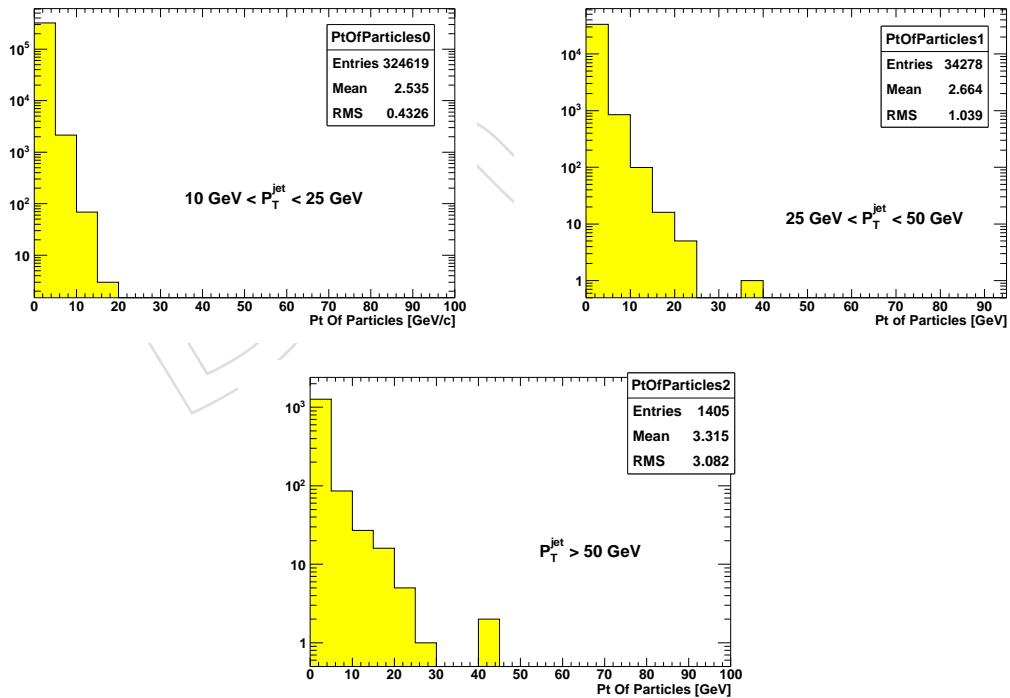


Figure 10: The  $p_T$  distribution of the stable particles in a jet for different jet  $p_T$  bins in PYTHIA Monte Carlo events.

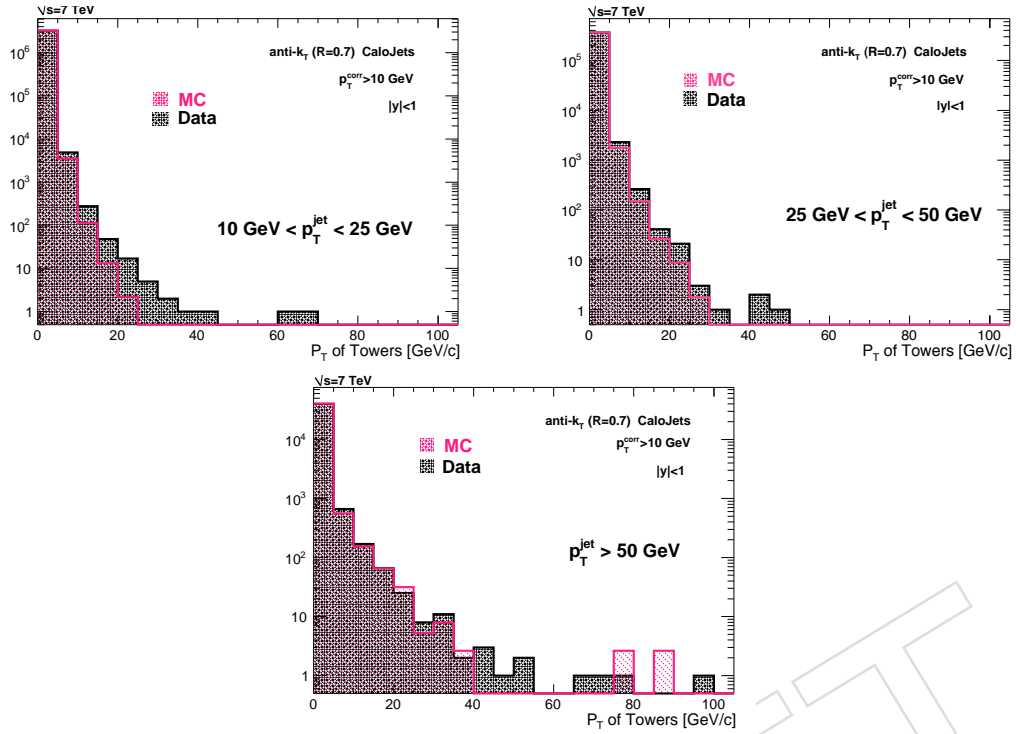


Figure 11: The  $p_T$  distribution of the towers in a jet for different jet  $p_T$  bins. The data are compared to the MC predictions.

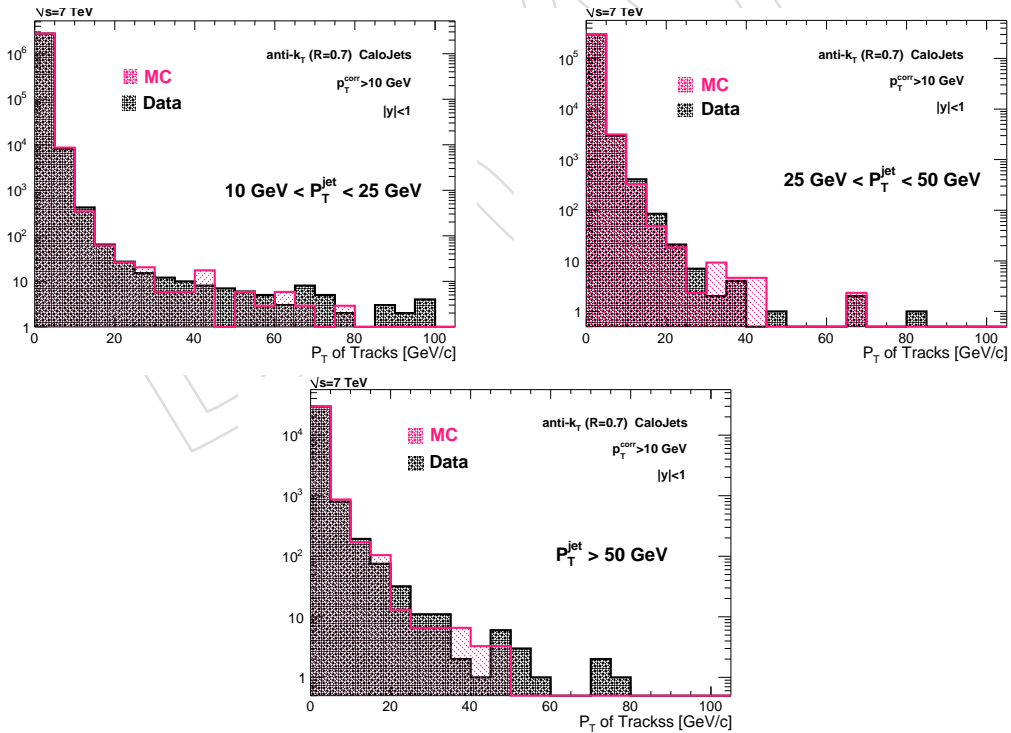


Figure 12: The  $p_T$  distribution of the tracks in a jet for different jet  $p_T$  bins. The data are compared to the MC predictions.

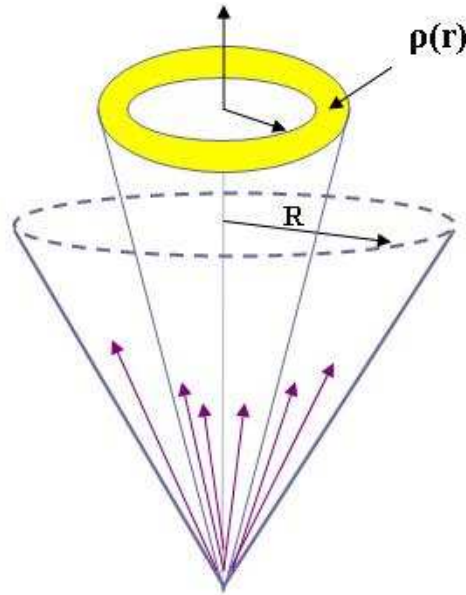


Figure 13: Definition of the differential jet shape,  $\rho(r)$ .

## 135 8 Definition of Jet Shapes

The jet shape is defined as the average fraction of the jet transverse momentum within a cone of a given size  $r$  around the jet axis,  $r = \sqrt{(y_i - y_j)^2 + (\phi_i - \phi_j)^2}$ , where  $i$  refers to the particle, calorimeter tower or track, and  $j$  to the jet. Jet shapes can be studied by using an integrated or a differential distribution. In the present study only two leading jets within  $|y| < 1$  are considered per event. All particles and calorimeter towers within distance  $R = \sqrt{(\Delta y)^2 + (\Delta \phi)^2} = 0.7$  from the jet axis are used. This large cone size ensures that most of the parent parton energy is included in the jet. The differential distribution,  $\rho(r)$ , is illustrated in Fig. 13. It is defined as the fraction of the jet transverse momentum contained inside an annulus of inner radius  $r - \delta r/2$  and outer radius  $r + \delta r/2$  around the jet axis, such that  $0 \leq r \leq R$ :

$$\rho(r) = \frac{1}{\delta r} \frac{1}{N_{jet}} \sum_{jets} \frac{p_T(r - \delta r/2, r + \delta r/2)}{p_T(0, R)}. \quad (4)$$

136 Above,  $N_{jet}$  denotes the total number of selected jets. In the numerator  $p_T$  is the sum of all  
 137 particles, tracks or towers in the distance range  $(r - \delta r/2, r + \delta r/2)$  from the jet axis. In the  
 138 denominator,  $p_T(0, R)$  is the scalar sum of transverse momenta of all the particles, tracks or  
 139 towers within the cone of radius  $R$ .

Similarly, the integrated jet shape (see Figure 14),  $\psi(r)$ , is defined as:

$$\psi(r) = \frac{1}{N_{jets}} \sum_{jets} \frac{p_T(0, r)}{p_T(0, R)} \quad (5)$$

140 where  $p_T(0, r)$  is the scalar sum of transverse momenta of all particles within the distance  $r$   
 141 from the jet axis with  $\psi(r = R) \equiv 1$ .

142 To calculate the jet shapes, we made histograms of transverse momentum in the appropriate  
 143 bin of  $r$  divided by the transverse momentum in the cone  $R = 0.7$ . The mean value of these

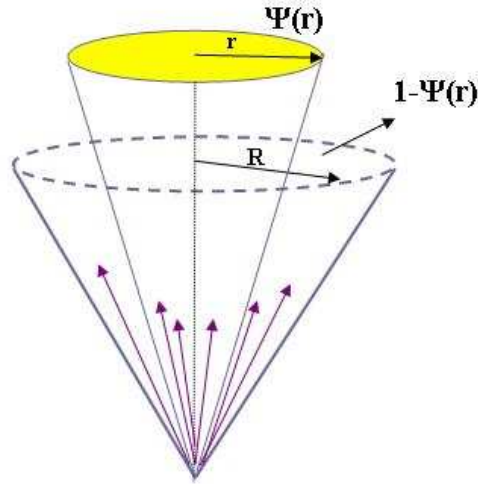


Figure 14: Definition of the integrated jet shape,  $\psi(r)$ .

144 histograms was then plotted as function of  $r$ . The statistical uncertainty on each point was  
 145 calculated as  $rms/\sqrt{N}$ , using the  $rms$  of the corresponding histogram and the number  $N$  of  
 146 jets in the bin. For the integrated shape the uncertainties at different  $r$  points are partially  
 147 correlated.

## 148 9 Raw Jet Shapes

149 Figure 15 and Figure 16 show the differential and integrated jet shapes for data events mea-  
 150 sured using calorimeter towers for various jet  $p_T$  bins. Most of the momentum is concentrated  
 151 within a small region around the jet axis. Jet shapes become narrower with the increasing  $p_T$   
 152 of the jet. The data are in good agreement with the calorimeter jetshapes predicted by PYTHIA  
 153 event generator using underlying event tune DW. The jetshapes measured using tracks is also  
 154 shown for both data and simulated events and show good agreement. The jetshapes measured  
 155 using tracks also show the the same trend, though they are slightly wider.

## 156 10 Jet Shape Corrections

157 Due to various detector effects, the measured (calorimeter) jet shapes are different than the true  
 158 (particle) jet shapes. Due to the magnetic field of CMS, charged particles with  $p_T < 0.9$  GeV  
 159 do not reach the calorimeter. In addition showers from particles interacting with the detector  
 160 material spread their energy over many calorimeter towers. The measured jet shapes must  
 161 be corrected for these detector effects. Correction factors were determined as a function of  
 162 distance from the jet axis using MC events before and after the CMS detector simulation. For  
 163 this approach to be valid, the MC simulation must describe the calorimeter response accurately.  
 164 Currents studies of the single particle response show that the data are well described by the  
 165 data [14]. The corrections have been determined using unmatched jets and are applied as a  
 166 function of distance from the jet axis.

167 The correction factors  $C_D(r)$  and  $C_I(r)$  for differential and integrated jet shapes are defined in  
 168 Equations 5 and 6, respectively:

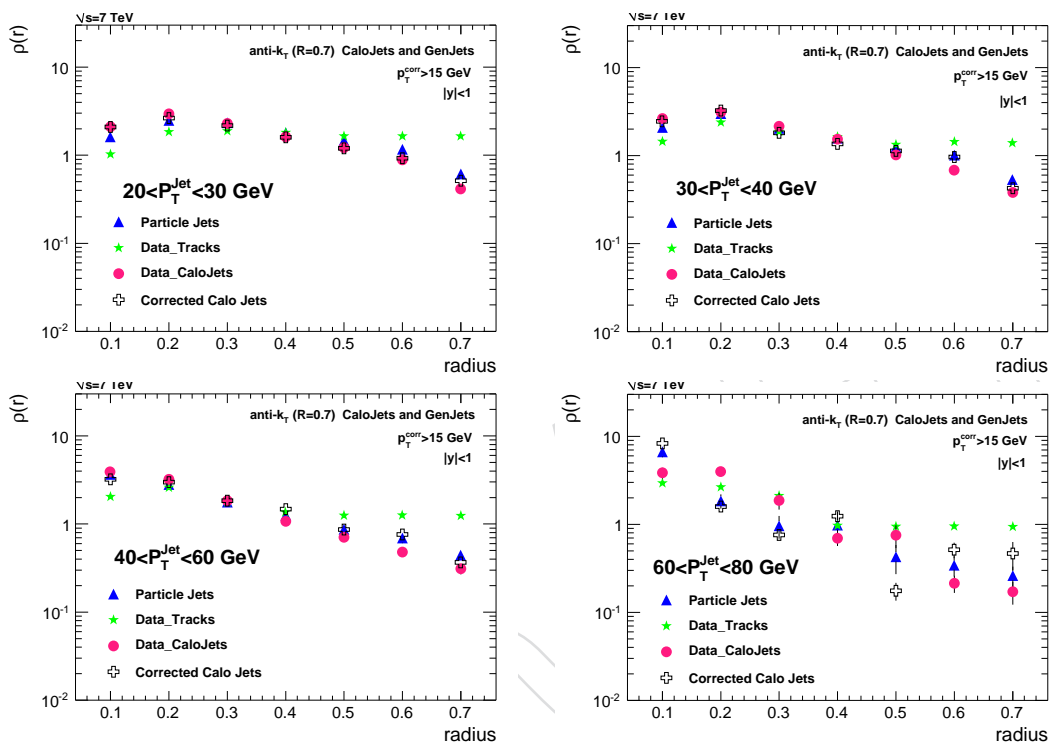


Figure 15: Differential jetshpes for jet in various  $p_T^{\text{Jet}}$  bins. The data are compared with PYTHIA predictions for both calorimeter jetshpes and track jetshpes. **Pelin: Can you remove the corrected and particle level jetshpes.**

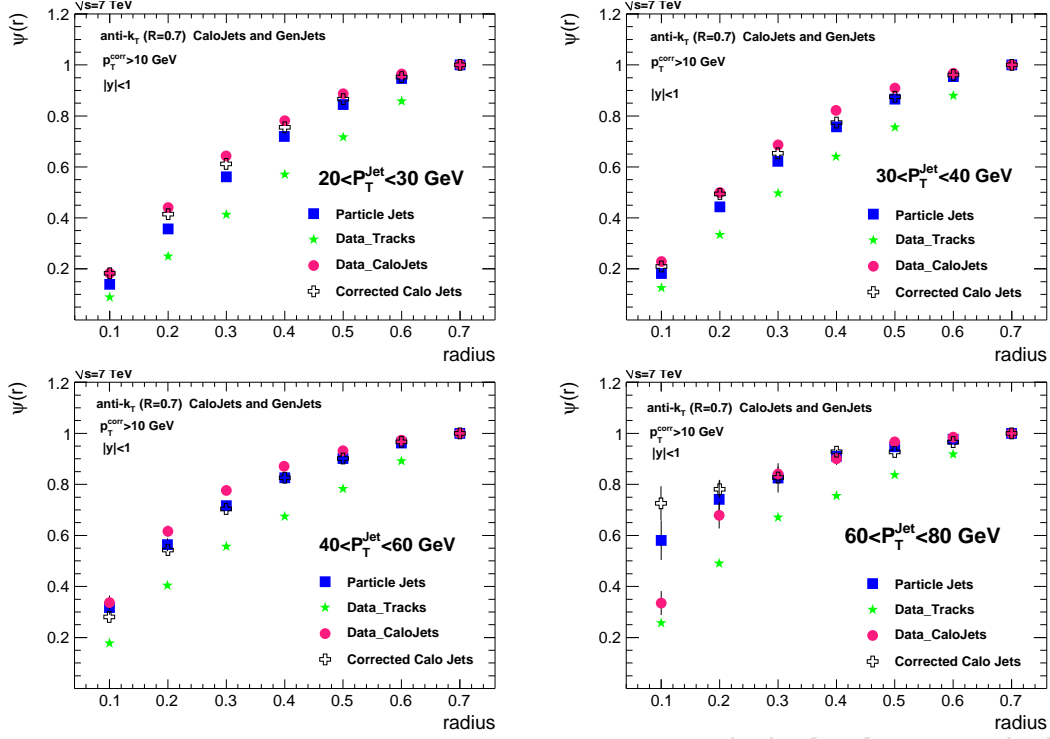


Figure 16: Integrated jetshpes for jet in various  $p_T^{\text{Jet}}$  bins. The data are compared with PYTHIA predictions for both calorimeter jetshpes and track jetshpes. **Pelin: Can you remove the corrected and particle level jetshpes**

Figure 17: Correction factors for differential jetshpes for jet in various  $p_T^{\text{Jet}}$  bins as determined from PYTHIA MC event generator.

Figure 18: Correction factors for integrated jetshpes for jet in various  $p_T^{\text{Jet}}$  bins as determined from PYTHIA MC event generator.

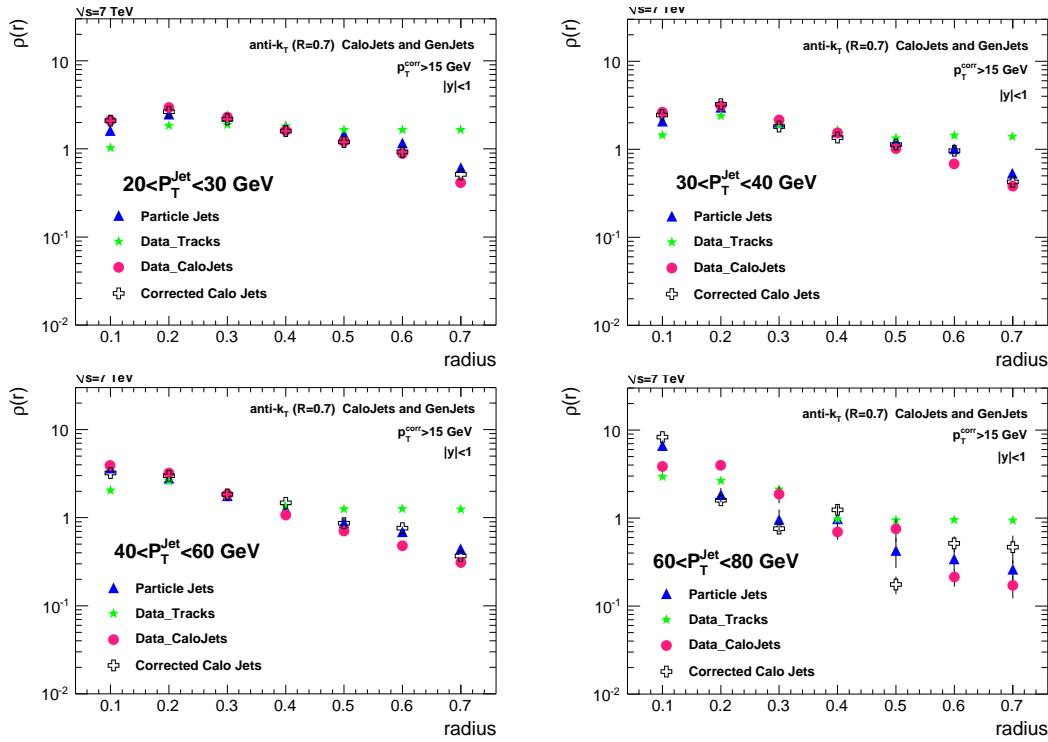


Figure 19: Particle level differential jetshpes for jet in various  $p_T^{\text{Jet}}$  bins. The data are compared with PYTHIA predictions. **Pelin: Can you remove the raw calorimeter and track jetshpes.**

$$C_D(r) = \rho_{MC}^{\text{PARTICLE}}(r) / \rho_{MC}^{\text{CAL}}(r) \quad (6)$$

$$C_I(r) = \psi_{MC}^{\text{PARTICLE}}(r) / \psi_{MC}^{\text{CAL}}(r) \quad (7)$$

169 where calorimeter towers and generated particles have been used to reconstruct differential  
 170  $\rho_{MC}^{\text{CAL}}(r)$ ,  $\rho_{MC}^{\text{PARTICLE}}(r)$  and integrated jet shapes  $\psi_{MC}^{\text{CAL}}(r)$ ,  $\psi_{MC}^{\text{PARTICLE}}(r)$  in different bins of jet  $p_T$ .

171 Measured calorimeter jet shpes are then used to determine the corrected differential jet shpes  
 172  $\rho^{\text{corrected}}(r) = C_D(r) \cdot \rho^{\text{CAL}}(r)$  and integrated jet shpes  $\psi^{\text{corrected}}(r) = C_I(r) \cdot \psi^{\text{CAL}}(r)$ .

173 The correction factors  $C_D(r)$  in Figure 17 do not show a significant dependence on jet  $p_T$  in  
 174 the region  $r < 0.5$ . They vary between 0.6 and 1.3 as a function of  $r$ , and between 1.3-2 for the  
 175 region  $r > 0.5$ . The correction factors for integrated jet shpes in Figure 18 vary from 0.9 to 1.06  
 176 for all radius and  $p_T$  bins. For the integrated distributions, the correction factors do not have a  
 177 strong dependence on jet  $p_T$ .

## 178 11 Corrected Jet Shapes

179 The corrected differential and integrated jet shpes are shown in Figures 19 and 20. Close to  
 180 the jet axis, the jet shape is dominated by collinear gluon emission, whereas at large distance  
 181 from the jet axis, the jet shape reflects large angle gluon emissions, which can be calculated  
 182 perturbatively. The jet shape  $\psi(r)$  increases faster with  $r$  for jets at larger  $p_T$  indicating that  
 183 these jets are more collimated.

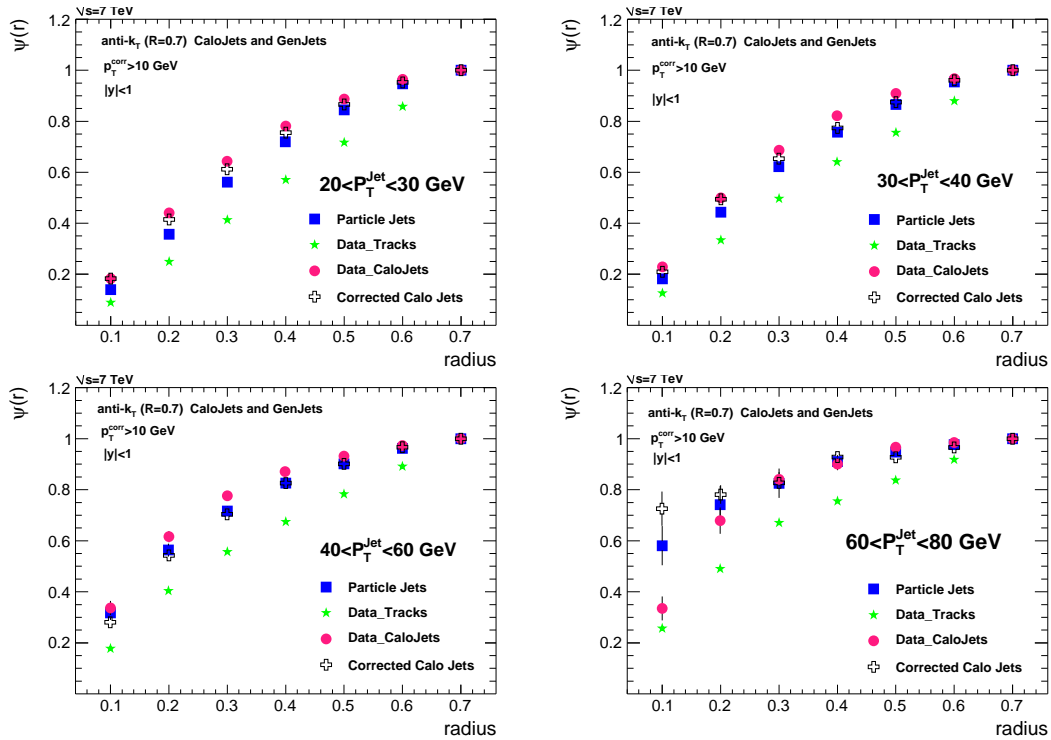


Figure 20: Particle level integrated jetshpes for jet in various  $p_T^{\text{Jet}}$  bins. The data are compared with PYTHIA predictions. **Pelin: Can you remove the raw and track jetshpes**

Figure 21: Differential jetshpes for jet in various  $p_T^{\text{Jet}}$  bins compared to PYTHIA MC predictions using different UE tunes

## 12 Sensitivity of Jet Shapes to Underlying Event Tunes

184

185 The energy from the underlying event (UE) contributes to jets and impacts the jet shapes. To  
 186 determine the sensitivity of jet shapes to the UE contribution, event samples were generated  
 187 using PYTHIA DW which has a smaller UE contribution than PYTHIA with tune DWT, which  
 188 is the CMS default setting [15]. These tunes are different extrapolations to  $\sqrt{s}=7$  TeV of the  
 189 same tune at the Tevatron energy  $\sqrt{s}=1.8$  TeV. The jet shapes for PYTHIA DWT and PYTHIA  
 190 DW are shown in Fig. 21 for the differential jet shapes and in Figure 22 for the integrated jet  
 191 shapes. At low jet  $p_T$ , one can observe the difference in jet shapes due to the UE contribution.  
 192 Underlying event contribution as a fraction of the jet  $p_T$  is larger at low  $p_T$  and at large radii.

## 13 Quark and Gluon Jet Shapes

193

194 Jet shapes are sensitive to quark and gluon jet contributions. The quark jets are narrower than  
 195 the gluon jets due to the coupling strengths for gluon emission which depend on the color

Figure 22: Integrated jetshpes for jet in various  $p_T^{\text{Jet}}$  bins compared to PYTHIA MC predictions using different UE tunes

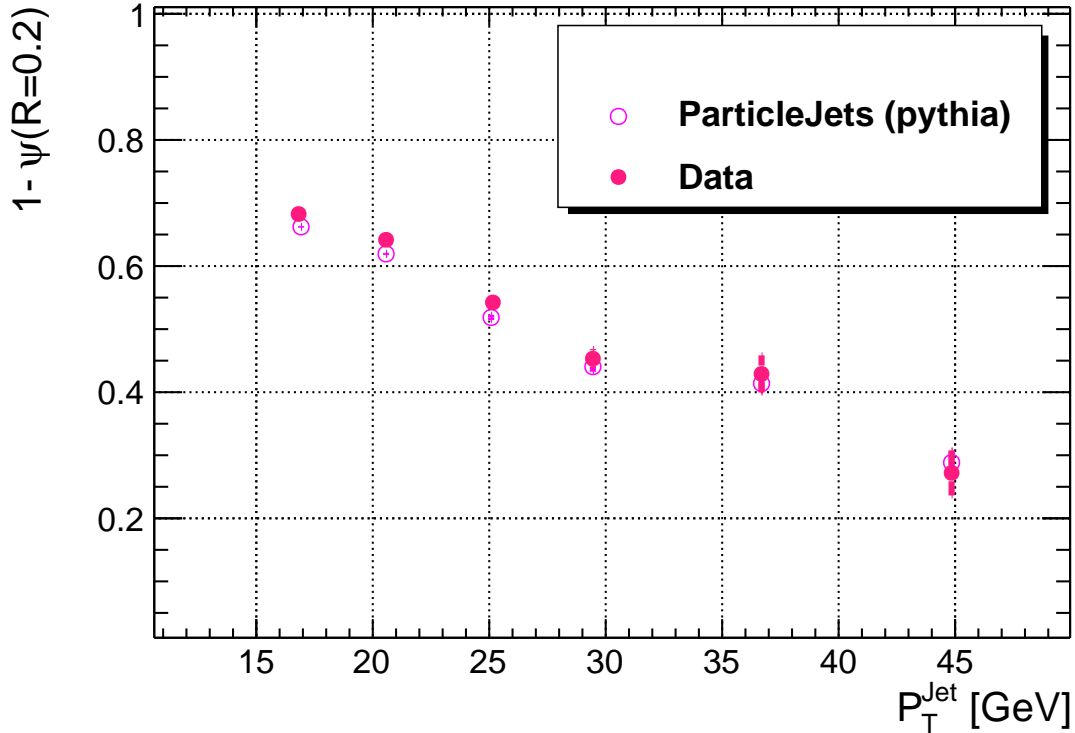


Figure 23: Jet transverse momentum fraction outside  $r=0.2$  regions.

196 factors  $C_F=4/3$  for radiating quarks and  $C_A=3$  for gluons. It is instructive to separate the jets by  
 197 the flavor and study their shapes. As shown above in Fig 1, the flavor composition of the jets  
 198 in QCD multi-jet sample changes with the transverse energy of the jets as the proton parton  
 199 distribution change with momentum fraction  $x$ . Fraction of jet momentum with  $r \leq 0.2$  is  
 200 shown in Fig. 23. The data are compared with parton shower+hadronization MC predictions  
 201 for quark and gluon jets. Tables 2, 3 and 4 provide details of the calculation of statistical and  
 202 systematic uncertainties for  $1 - \psi(r = 0.2)$  in all  $p_T$  bins. The simulated jets are classified as  
 203 quark or gluon jets by matching the particle jets with a parton from  $2 \rightarrow 2$  scattering within  
 204  $\Delta R < 0.5$  in  $(y, \phi)$  space. The MC predicts that the measured jet shapes are dominated by  
 205 contributions from gluon initiated jets at low jet  $p_T$  while contributions from quark initiated jets  
 206 become important at high jet  $p_T$ . MC also predicts that the both quark and gluon jets become  
 207 narrower with increasing jet  $p_T$ . The data are in qualitative agreement with these predictions.

## 208 14 Systematic Uncertainties

209 The main sources of systematic uncertainties include:

- 210 • Jet energy scale
- 211 • Transverse shape of calorimeter showers
- 212 • Non-linearity of calorimeter response
- 213 • Jet fragmentation

214 The uncertainties arising from jet energy and position resolution, and from event selection cuts  
 215 are expected to be negligible compared to the sources listed above and are not considered.

Figure 24: The fractiona change in the differential jetshapes due to uncertainty in the jet energy scale determined by changing the jet energy scale by  $\pm 10\%$  independent of jet  $p_T$  and  $y$ .

Figure 25: The fractiona change in the integrated jetshapes due to uncertainty in the jet energy scale determined by changing the jet energy scale by  $\pm 10\%$  independent of jet  $p_T$  and  $y$ .

## 216 14.1 Jet Energy Scale

217 Current expectation of the JES uncertainty at start up is  $\pm 10\%$  [16]. Changing the JES correction  
 218 within its uncertainty changes the jet shapes as jets migrate between  $p_T$  bins. Jet shapes vary  
 219 slowly with jet  $p_T$  and thus this effect is expected to be small. To determine the impact on the jet  
 220 shapes, we changed the  $p_T$  of the jet by  $\pm 10\%$  and repeated the whole analysis. The comparison  
 221 between the default JES corrections and the modified corrections is shown in Figure 24. The  
 222 corresponding systematic uncertainties on the differential jet shape are 10% at  $r=0.1$  and  $< 5\%$   
 223 at  $r = 0.2$  for all jet  $p_T$ . At larger  $r \geq 0.5$  they are  $< 20\%$ .

224 The uncertainties on the integrated jet shape are 10% at  $r=0.1$ , 5% at  $r=0.2$  for  $p_T < 100$  GeV, and  
 225 decrease as a function of  $r$ . They are  $< 2\%$  at  $r=0.1$  for  $p_T > 100$  GeV and negligible at  $r > 0.1$ ,  
 226 as shown in Figure 25. The systematic uncertainty at  $r=0.7$  is 0 by definition of the integrated  
 227 jet shape.

## 228 14.2 Jet Fragmentation

229 Because the calorimeter response depends on the momenta of the particles in the jets, mod-  
 230 eling of jet fragmentation contributes to the uncertainty on the corrected jet shapes. Uncer-  
 231 tainties due to the fragmentation model can be estimated by comparing the correction factors  
 232 determined using PYTHIA and HERWIG events.. The model of the underlying event used in  
 233 HERWIG++ is described in [17]. Particle level differential and integrated jet shapes in PYTHIA  
 234 DWT and HERWIG++ 2.2 [18] are shown in Figure 26 and Figure 27. Their observed difference  
 235 is less than 5% at  $r < 0.3$ .

236 To determine the systematic uncertainty due to modeling of jet fragmentation we compared  
 237 PYTHIA DWT and HERWIG++ differential jet shape correction factors, shown in Figure 28.  
 238 They agree to  $< 10\%$  for  $r \leq 0.2$ , however, the differences can be as large as 30 – 40% at  $r \geq 0.5$ .  
 239 Note that the jet energy fraction at large  $r$  is small, which makes uncertainties on the differential  
 240 jet shape measurement large in this region.

241 Comparisons of the integrated jet shape correction factors for PYTHIA DWT and HERWIG++  
 242 are shown in Figure 29. They agree within 5% (2%) at  $r=0.1$  (0.2) for  $60 < p_T < 80$  GeV. For  
 243  $p_T > 80$  GeV the differences range between 5 – 10% at  $r=0.1$  and are less than 5% at  $r=0.2$ .  
 244 These differences decrease with increasing radius  $r$  for all jet  $p_T$ .

245 The correction factors have been also compared for PYTHIA DWT and PYTHIA DW simula-  
 246 tions. The differences are less than 20% at  $r=0.1$  and  $< 10\%$  at  $r = 0.2$ . For differential jet  
 247 shapes at large  $r$ , they can be as large as 20 – 30%. For integrated jet shapes, they become

Figure 26: Particle level differential jetshapes as predicted by PYTHIA and HERWIG event gen-  
 erators for selected  $p_T^{\text{Jet}}$  bins.

Figure 27: Particle level integral jetshapes as predicted by PYTHIA and HERWIG event generators for selected  $p_T^{\text{Jet}}$  bins.

Figure 28: Corrections factor for differential jetshapes as determined from PYTHIA and HERWIG event generators for selected  $p_T^{\text{Jet}}$  bins.

248 smaller for the high  $p_T$  jets and decrease with increasing  $r$ . The comparisons of correction factors for PYTHIA DWT and PYTHIA DW are shown in Figure 30 for differential jet shapes and  
249  
250 in Figure 31 for integrated jet shapes.

### 251 14.3 Non-linearity of Calorimeter Response and Transverse Shower Profile

252 The uncertainties due to CMS calorimeter simulation can be estimated by comparing track jet  
253 shapes with calorimeter jet shapes in simulated and collider data. Here we assume that track  
254 reconstruction inefficiency and fake rate are small in both data and MC and have negligible  
255 effect on track jet shapes. In addition, it is assumed that any difference in calorimeter response  
256 to photons in data and MC is much smaller than possible difference in calorimeter response to  
257 hadrons. The track jetshapes are compared to calorimeter jetshapes in Figure ?? for data and  
258 the PYTHIA predictions. These ratios, under above assumptions, show the effective calorimeter  
259 response to particles as a function of  $r$ . The two responses are very close. The difference is  
260 assigned as the systematic uncertainty on the observed jetshapes. The scale factor  $SF$  as  
261 defined below is very close to 1.0, showing that calorimeter simulation describes the observed  
262 calorimeter response very well. The difference from unity is assigned as systematic uncertainty.  
263 and the deviation from unity is assigned as the systematic uncertainty. Analogous procedure  
264 is used for the integrated jet shapes (see Fig. 33).

$$SF = \frac{R^{DATA}}{R^{MC}} \quad \text{where} \quad R^{MC} = \frac{TrackJetShape}{CaloJetShape} \Big|_{MC}, \quad R^{DATA} = \frac{TrackJetShape}{CaloJetShape} \Big|_{DATA} \quad (8)$$

## 265 15 Conclusions

266 We have measured differential and integrated jetshapes of the jets with  $15 < p_T < 150$  GeV in  
267  $|y| < 1.0$  region produced in  $pp$  collisions at  $\sqrt{s} = 7$  TeV. These jets become narrower with  
268 increasing jet transverse momentum, in good agreement with QCD inspired event generators,  
269 PYTHIA and HERWIG. The observed jetshapes are closer to gluon jetshapes at low  $p_T$  and tend  
270 toward quark jetshapes at high  $p_T$ . A comparison of these jetshapes with different PYTHIA  
271 tunes shows that these data prefer **CW** tune.

272 Several sources of systematic uncertainties were investigated, arising from jet energy calibration,  
273 jet fragmentation, calorimeter response and transverse showering, as a function of jet  $p_T$

Figure 29: Corrections factor for differential jetshapes as determined from PYTHIA and HERWIG event generators for selected  $p_T^{\text{Jet}}$  bins.

Figure 30: Corrections factor for differential jetshapes determined using two different tunes of the PYTHIA event generator for selected  $p_T^{\text{jet}}$  bins.

Figure 31: Corrections factor for integral jetshapes determined using two different tunes of the PYTHIA event generator for selected  $p_T^{\text{jet}}$  bins.

274 and distance from jet axis  $r$ . The systematic uncertainty is dominated by overall jet energy  
275 scale, jet fragmentation and calorimeter simulation effects. The total systematic uncertainty at  
276  $r=0.2$  is 12% at  $p_T = 60$  GeV, decreasing to 4% at jet  $p_T = 1$  TeV.

DRAFT

Figure 32: Effective calorimeter response to particles in data and simulated events as function of distance  $r$  for selected  $p_T^{\text{jet}}$

Figure 33: Effective calorimeter response to particles in data and simulated events as function of distance  $r$  for selected  $p_T^{\text{jet}}$

GeV	$N^{jets}$	$N_p$	$\langle \psi(r = 0.2) \rangle$	$rms$	$\sigma = rms / \sqrt{N_p}$	$\sigma / \langle \psi(r = 0.2) \rangle$ (%)
15-20	5313					
20-30	4333					
30-40	1147					
40-50	403					
50-60	210					
60-80	101					
80-100	41					
100-	16					

Table 1: Number of jets before and after prescale, and mean and rms values of the  $p_T$  fraction histograms at  $r=0.2$  in  $10 \text{ pb}^{-1}$  for all  $p_T$  jet bins which were analyzed. Statistical errors are listed for the corresponding jet  $p_T$  using prescaled event numbers.

Table 2: Different sources of systematics for  $\psi(r = 0.2)$  listed as percentage contributions for all jet  $p_T$  bins for  $10 \text{ pb}^{-1}$  of integrated luminosity. Total systematics is a quadrature sum of fragmentation, jet energy scale, showering and  $E/p$  contributions.

$p_T$ (GeV)	Fragmentation(%)	JES(%)	Showering(%)	$E/p$ (%)	TotalSys.(%)
-------------	------------------	--------	--------------	-----------	--------------

Table 3: Absolute error on  $1 - \psi(r = 0.2)$  represents quadratic sum of systematic and statistical uncertainties for  $10 \text{ pb}^{-1}$  of integrated luminosity.  $I(r = 0.2)$  refers to the integrated correction factors at  $r=0.2$ .

$p_T$ GeV	Raw $\psi(r = 0.2)$	$I(r = 0.2)$	$1 - \psi(r = 0.2)$	AbsErr
15 - 20	0.66	0.90	0.41	0.072

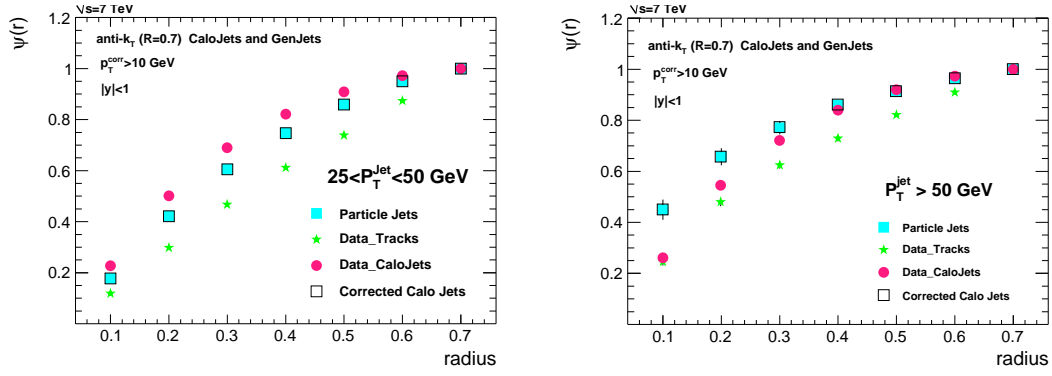


Figure 34: Corrected Integrated JetShapes

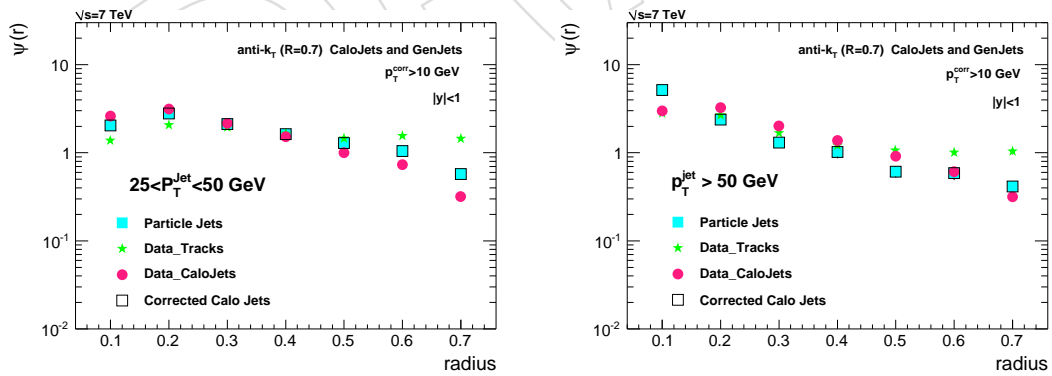


Figure 35: Corrected Integrated JetShapes

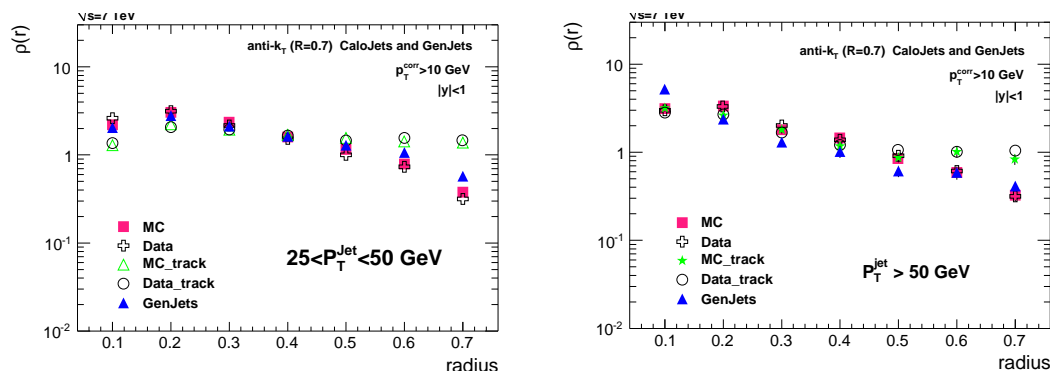


Figure 36:

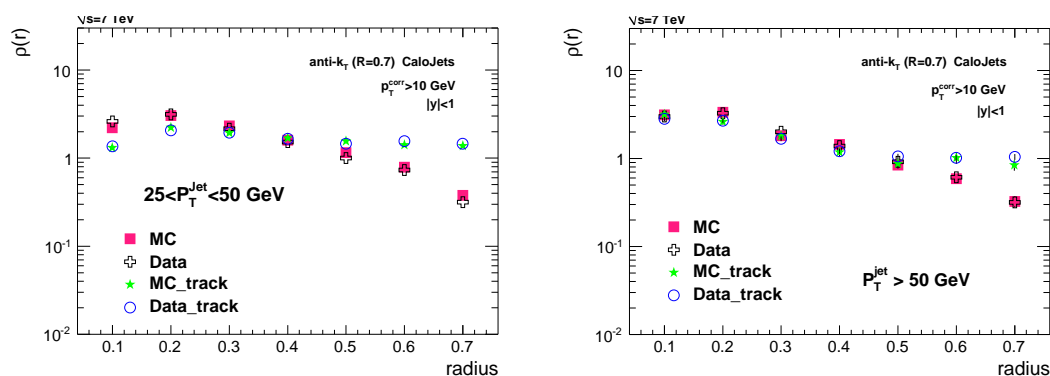


Figure 37: Differential JetShapes

## References

277

278 [1] S. D. Ellis, Z. Kunszt, and D. E. Soper, "Jets at hadron colliders at order  $\alpha_s^3$ : A  
279 Look inside", *Phys. Rev. Lett.* **69** (1992) 3615–3618, arXiv:hep-ph/9208249.  
280 doi:10.1103/PhysRevLett.69.3615.

281 [2] M. H. Seymour, "Jet shapes in hadron collisions: Higher orders, resummation and  
282 hadronization", *Nucl. Phys.* **B513** (1998) 269–300, arXiv:hep-ph/9707338.  
283 doi:10.1016/S0550-3213(97)00711-6.

284 [3] CDF Collaboration, F. Abe et al., "A Measurement of jet shapes in  $p\bar{p}$  collisions at  
285  $\sqrt{s} = 1.8$  TeV", *Phys. Rev. Lett.* **70** (1993) 713–717.  
286 doi:10.1103/PhysRevLett.70.713.

287 [4] D0 Collaboration, S. Abachi et al., "Transverse energy distributions within jets in  $p\bar{p}$   
288 collisions at  $\sqrt{s} = 1.8$  TeV", *Phys. Lett.* **B357** (1995) 500–508.  
289 doi:10.1016/0370-2693(95)00889-S.

290 [5] CDF Collaboration, D. E. Acosta et al., "Study of jet shapes in inclusive jet production in  
291  $p\bar{p}$  collisions at  $\sqrt{s} = 1.96$  TeV", *Phys. Rev.* **D71** (2005) 112002,  
292 arXiv:hep-ex/0505013. doi:10.1103/PhysRevD.71.112002.

293 [6] H1 Collaboration, C. Adloff et al., "Measurements of transverse energy flow in deep  
294 inelastic scattering at HERA", *Eur. Phys. J.* **C12** (2000) 595–607,  
295 arXiv:hep-ex/9907027. doi:10.1007/s100520000287.

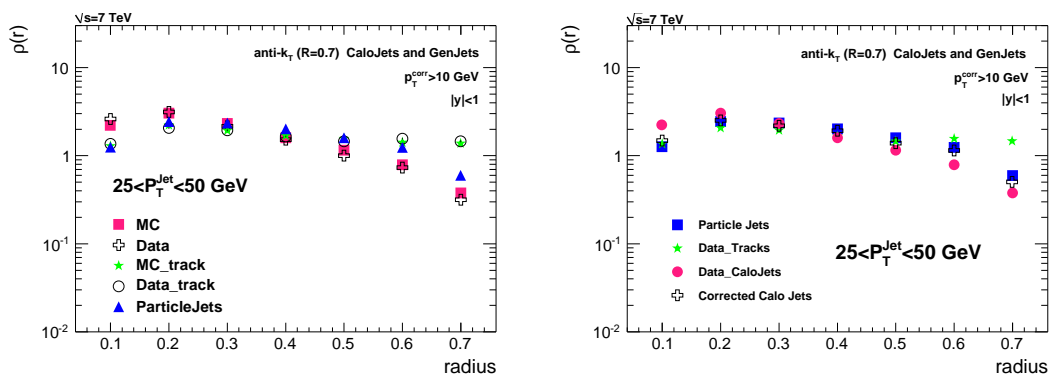


Figure 38:

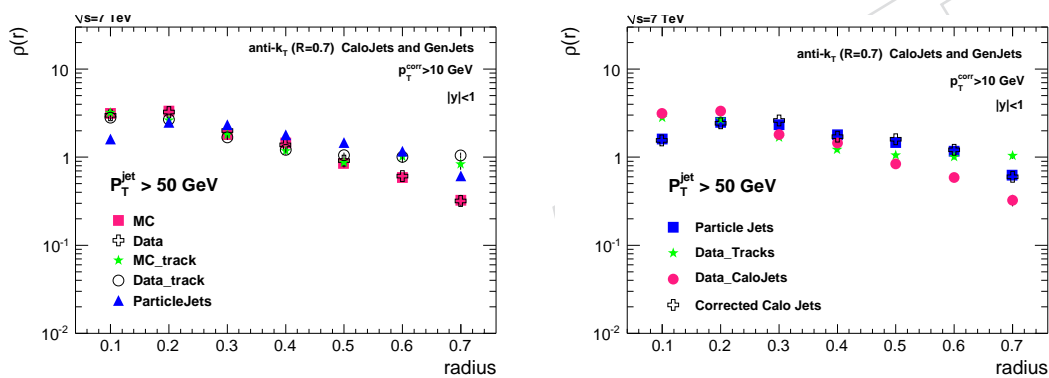


Figure 39:

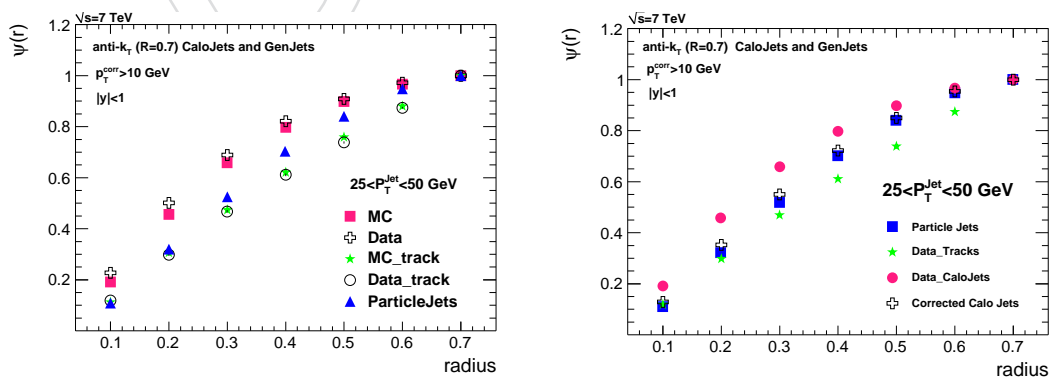


Figure 40:

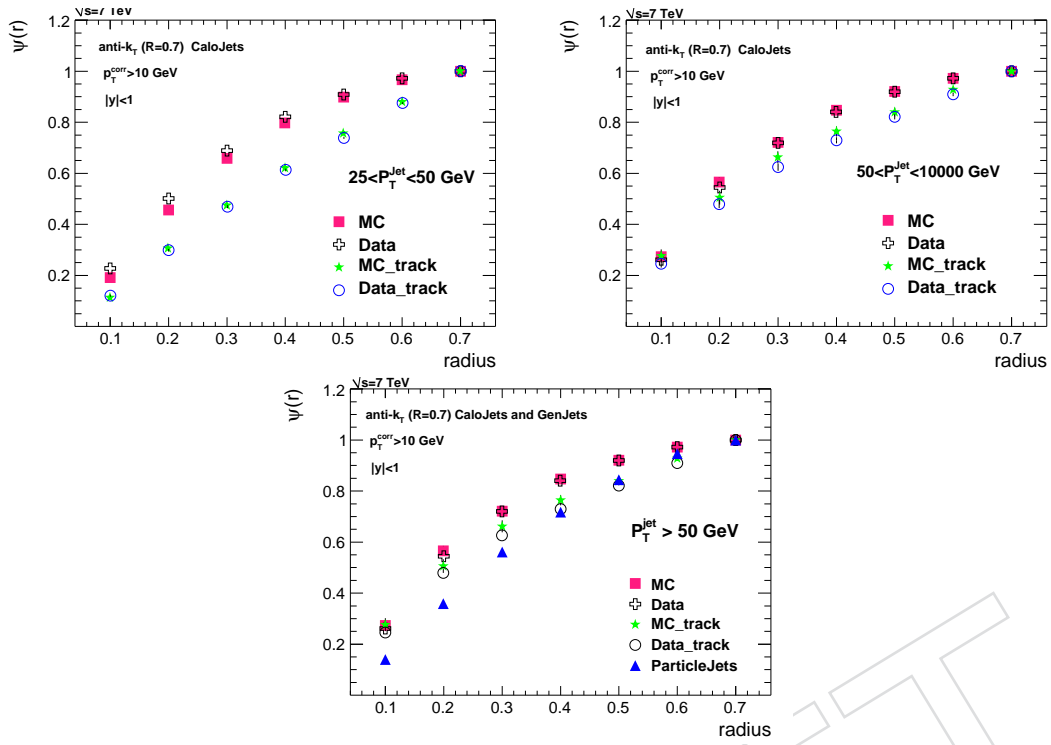


Figure 41:

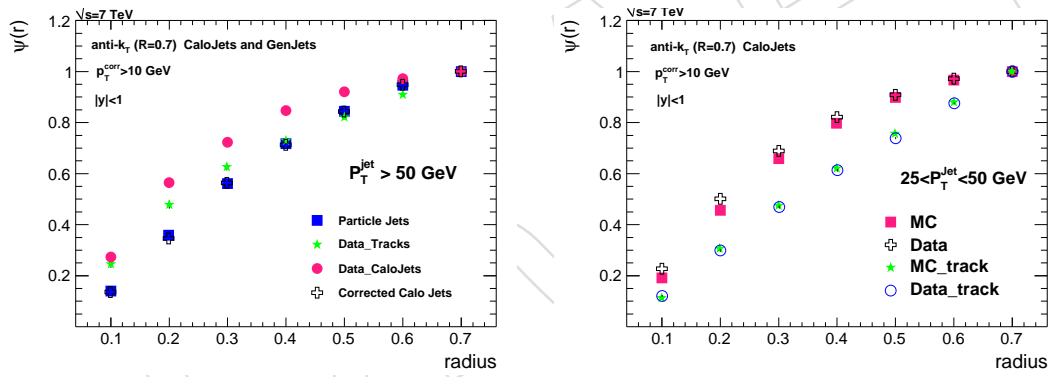


Figure 42:

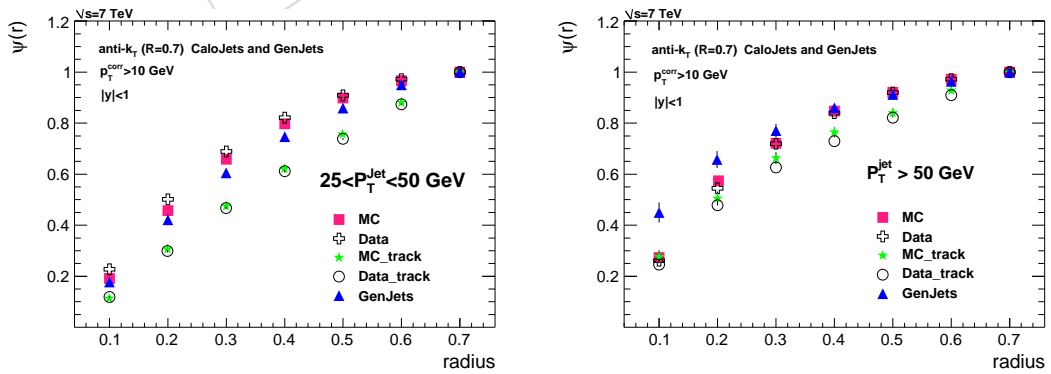


Figure 43:

- 296 [7] **ZEUS** Collaboration, J. Breitweg et al., “Measurement of jet shapes in high- $Q^2$  deep  
297 inelastic scattering at HERA”, *Eur. Phys. J.* **C8** (1999) 367–380, arXiv:hep-ex/9804001.  
298 doi:10.1007/s100520050471.
- 299 [8] **CMS** Collaboration, “The Compact MUon Solenoid (CMS) Technical Proposal”,  
300 CERN/LHCC 94-38.
- 301 [9] **CMS** Collaboration, “CMS TDR4”, CERN/LHCC 97-33.
- 302 [10] **CMS** Collaboration, “CMS TDR2”, CERN/LHCC 97-31.
- 303 [11] The coordinate system used at CMS is defined as follows: the  $x$ -axis points horizontally  
304 outside the LHC ring, the  $y$ -axis points upwards, and the  $z$ -axis is aligned with the  
305 nominal beam direction. The azimuthal angle is  $\phi$  and the polar angle is  $\theta$ . The transverse  
306 momentum  $P_T$  is defined as a projection of a particle momentum  $P$  on the  $xy$ -plane,  
307  $P_T = P \cdot \sin \theta$ . The rapidity is defined as  $y = \frac{1}{2} \log \frac{E+P_z}{E-P_z}$ , where  $E$  denotes the energy and  
308  $P_z$  is the component of the momentum along the  $z$  direction.
- 309 [12] G. P. Salam, “A Practical Seedless Infrared Safe Cone Algorithm”, arXiv:0705.2696.
- 310 [13] M. Cacciari, G. P. Salam, and G. Soyez, “The anti- $k_T$  jet clustering algorithm”, *JHEP* **04**  
311 (2008) 063, arXiv:0802.1189. doi:10.1088/1126-6708/2008/04/063.
- 312 [14] **CMS** Collaboration, S. Sharma et al., “Single tracks in CMS data”, CMS.
- 313 [15] **CMS** Collaboration, “The Underlying Event at LHC”, CMS-Note-2006/067.
- 314 [16] **CMS** Collaboration, “Plans for Jet Energy Corrections at CMS”, CMS-PAS-JME-007-002.
- 315 [17] M. Bahr, S. Gieseke, and M. H. Seymour, “Simulation of multiple partonic interactions in  
316 Herwig++”, *JHEP* **07** (2008) 076, arXiv:0803.3633.  
317 doi:10.1088/1126-6708/2008/07/076.
- 318 [18] M. Bahr et al., “Herwig++ 2.2 Release Note”, arXiv:0804.3053.